CIMAC CONGRESS 25
ZURICH, MAY 19 – 23, 2025

2025 | 269

Ignition and combustion behavior of H2 / CH4 blends at conditions relevant for large engines

Visualizations

Silas Wüthrich, University of Applied Sciences and Arts Northwestern Switzerland

German Weisser, WinGD
Patrick Albrecht, University of Applied Sciences and Arts Northwestern Switzerland
Kai Herrmann, University of Applied Sciences and Arts Northwestern Switzerland

ABSTRACT

The use of fuels with significantly lower net carbon emissions is a prerequisite for compliance with the greenhouse gas (GHG) reduction targets set out in the Paris Agreement mainly for land-based applications as well as the GHG reduction strategy of the International Maritime Organization (IMO) for international shipping. Besides the planned changeover to renewable fuels such as hydrogen (resp. ammonia or methanol as hydrogen carrier), methane/hydrogen blends (as carbon-reduced fuel) can be considered a promising solution for immediate use in existing gas and dual-fuel engines, at least during a transitional period.

Since pure hydrogen is known for its very short ignition delay, high burn-rates and low storage density, its blending into conventional fuels such as natural gas represents certain challenges and has been investigated earlier for a wide range of applications. Specific changes to the engine and combustion control systems were found to be required for safe operation and to fulfil the emission standards on automotive to heavy-duty applications already. For large engine applications, such need for adjustments must be expected to be even higher; this triggered the present fundamental investigations of combustion of methane/hydrogen blends, conducted under conditions relevant for large engines on the optically accessible test bench "Flex-OeCoS".

The “Flex-OeCoS” has been specifically designed to allow the application of optical measurement methods for acquiring ignition and flame propagation data on a wide range of operational parameters. It is capable to achieve engine relevant compression/combustion pressures and temperatures at variable speeds and its very elaborate operating concept allows adjusting main parameters such as pressure, temperature and turbulence intensity at start of combustion individually and with a high level of accuracy and reproducibility.

The present work starts with an outline of the experimental setup and the parameter variations studied. The results contain characteristic data for the different fuel blends in terms of cylinder pressure and combustion-related quantities derived from it: heat release rate, ignition delay, and fuel conversion rates. These data are supported by simultaneously acquired high-speed imaging data in terms of Schlieren and OH* Chemiluminescence. Those optical measurement methods not only allow visualizing features important for the better understanding of combustion such as flame interactions, but also provide the basis for determining valuable quantitative information such as apparent flame speed and first flame onset timing (true ignition delay). Emission measurements round off these investigations and show how both, regulated pollutant such as NOx, and total GHG emissions are affected by hydrogen enrichment and what mitigation measures may be required in order to achieve the overall targets of continued compliance and reduction of GHG emissions.

The results of these investigations are expected to serve as an excellent basis for the identification of ranges of hydrogen blending into methane applicable on existing gas and dual-fuel engines, requirements for enabling large engines to cope with hydrogen addition and initial specification of combustion control systems. This ultimately allows determining the potential of solutions on such basis to contribute to the decarbonization targets of the sectors in which those engines are applied.

1 INTRODUCTION

The goal of a carbon-neutral society is set out in the Paris Agreement, a legally binding international treaty on climate change, which aims to keep the global average temperature increase well below 2°C above pre-industrial levels and to step up efforts to limit the temperature increase to 1.5°C, thus responding to the findings of the Intergovernmental Panel on Climate Change [1]. While the Paris Agreement mainly aims at land-based applications, the International Maritime Organization (IMO) has set out a greenhouse gas (GHG) reduction strategy for international shipping [2]. Overall, it is imperative that both private and industrial sectors reduce their GHG emissions towards zero over the course of this century. Wherever possible, electrification based on renewable energies is the most efficient approach to achieve this goal.

On the other hand, due to the limited energy density of batteries, direct use of electricity is limited or not possible in all segments. This is particularly the case for the marine sector, where – apart from certain niche applications such as ferries or short sea shipping – the transition from fossil to sustainable energy carriers with sufficiently high energy density is the only viable option for decarbonization. Such energy carriers are associated with the lowest impact in terms of cargo capacity loss and allow the continued use of large Internal Combustion Engines (ICE), which have proven to be the most efficient and reliable means of marine propulsion power generation, over many decades. Obviously, these engines need to be further developed, adapted to, and optimized for the application of those energy carriers.

Various technology paths for ICE and fuel systems for future propulsion of ships have been investigated. For the substitution of fossil fuels, besides biogenic fuels, synthetic ammonia (NH_3), methanol and methane (CH_4) were identified as the most viable candidates for an economically feasible route to decarbonization [3]. Of course, these fuels must be produced via renewable energy, and only ammonia can be considered as fully carbon-free. Since methanol and methane still contain carbon, the carbon needed for their production must come from non-fossil sources to be considered carbon-neutral. All possible options regarding non-fossil fuels – including “green” hydrogen (H_2) for certain applications – have advantages and disadvantages in terms of suitability, handling, efficiency, cost, safety, environmental risks, etc. In particular, ammonia has recently gained increasing attention and is being touted by various stakeholders as one of the most promising future fuels. Various studies have investigated the potential for application in shipping from a cost and production point of view [4-9]. Although ammonia is a well-known substance for centuries, it has so far mainly been used to produce fertilizers. In terms of its use as an engine fuel, a transition phase up to 2050 is expected. In the meantime, the share of liquefied natural gas (LNG) can be expected to further increase, as the use of LNG already offers significant benefits regarding GHG emissions, compared to traditional liquid marine fuels.

Current concepts of gas-fueled engines are seen as a good basis for future solutions designed for operation on such alternative fuels. Even though a transition to alternative fuels such as ammonia will take place, the current fleet can be used to reduce the CO_2 emissions when drop-in fuels are available. In best cases, the engine control systems only need a “software upgrade” with a correct parameter set to use such fuels. On the hardware side, adoption of the fuel delivery system and a new turbocharger matching could probably be needed depending on change of fuel and air-fuel equivalence ratio target. Hydrogen enriched methane could be such a drop in fuel. Thus, the influence of hydrogen on ignition and combustion has to be examined under conditions relevant for marine engine applications. A range of complex processes involved such as flow field conditions, mixing properties, ignition, combustion onset, and flame propagation must be considered in this context.

An optically accessible experimental test facility (the so-called “Flex-OeCoS”) providing engine relevant operating conditions was used to fundamentally examine premixed homogeneous combustion ignited by a dodecane pilot. The investigations cover operating conditions across a broad range in terms of air-fuel equivalence ratio from $\lambda = 1.0$ to 2.5, engine loads from 10% to 80%, and compression temperatures from around 850 K to 950 K. The influence of different operating parameters such as mixture charge composition or intake temperature has been investigated. High speed imaging and typical combustion-relevant variables are given such as ignition delay, combustion onset, flame propagation speed, heat release, and exhaust gas composition.

2 EXPERIMENTAL SETUP, MEASUREMENT PROCEDURE, AND ANALYSIS

The optically accessible test facility Flex-OeCoS enables the examination of premixed pilot fuel ignited dual-fuel combustion processes in a range of IC engine relevant operational parameters [10]. Both operating and boundary condition data can be acquired with a temporal resolution of more than 10 per degree crank angle (deg CA). In addition to permanently carried out pressure measurements, the temperature distribution (by means of fine-wire thermocouples at various points to determine the compression temperature T_c) and the turbulent flow

field (using high-speed PIV) have been extensively characterized in previous studies [11]. The adaptable setup with flexible operating modes has already been used for a large variety of dual-fuel combustion process investigations [12 -17].

2.1 Test facility Flex-OeCoS

Figure 1 shows the working principle of the Flex-OeCoS test rig: One cylinder of a motor driven engine block feeds a mixture charge into an optical combustion chamber (Ø60 mm×20 mm), providing maximum optical access through rectangular and round sapphire windows at each side. Two intake valves (Ø16 mm) are located on the working cylinder, which is equipped with a flat-top piston. Two exhaust valves (Ø16 mm) are positioned on top of the combustion chamber, where a central bore at the top allows mounting of a pilot fuel injector, spark plug or pre-chamber. Various pressure sensors are implemented at different locations, and the entire head is thermally conditioned to achieve stable conditions during the aperiodic operation.

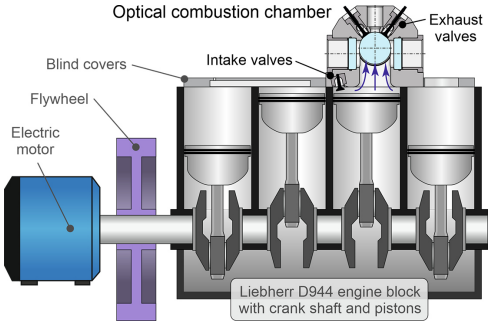

Figure 1. Concept of the Flex-OeCoS test facility and optical combustion chamber replacing the cylinder head on top of the working cylinder.

The Flex-OeCoS test facility features adaptable operation at IC engine relevant conditions: peak pressures in continuous operation of up to 260 bar (from boost-adjustable compression pressure p_c up to 160 bar), end of compression temperatures (T_c) between 700 and 1050 K by intake conditioning, and tunable flow (turbulence grades) depending on motor speed (n) of typically 300 – 1000 rpm. An overview of relevant test facility specifications is given in Table 1.

Independent pneumatic intake and exhaust valve actuators provide high variability in terms of Otto-Miller or Atkinson cycles. Moreover, pilot fuel injection settings (pressure, start, and duration) as well as mixture charge composition, by gas introduction in the air intake pipe close to the intake valve, can be freely adjusted.

Table 1 Test facility specifications

Dimensions, Operating Parameter		
Working cylinder bore	Ø 130	[mm]
Stroke length	150	[mm]
Connecting rod length	237.1	[mm]
Displacement (working cylinder)	1990	[cm^3]
Compression ratio	13.02	[-]
Optical access main chamber diameter	Ø 60	[mm]
Possible engine speed range	300 - 1000	[rpm]
Turbulence intensity u'/c_m @ 600 rpm [10]	1.2	[-]
Intake boost pressure p_b	0 - 6.8	[bar]
Compression pressure	30 - 160	[bar]
Max. cylinder pressure	260	[bar]
Intake air preheating	20 - 250	[°C]
Compression end temperature (pure air)	700 - 1050	[K]

2.2 Optical setup, methodology and post-processing

As illustrated in Figure 2, simultaneous high-speed Schlieren/OH* chemiluminescence was applied to investigate pilot combustion, combustion transition, ignition processes, turbulent flame front propagation, as well as abnormal combustion characteristics such as pre-ignition and flame quenching. Image acquisition was performed by means of two high-speed cameras: The chemiluminescence of the OH* radical as indicator of inflammation was acquired simultaneously with the Schlieren signal indicating vaporized and burned phases within the main chamber. The spatial resolution has been set to 512x544 pixels for the given 60×60 mm, covering the entire optical window and resulting in a frame rate of 36 kHz for the typical motor speed of n = 600 rpm, corresponding to 0.1 deg CA.

The images acquired are superimposed for visualizing the key processes involved and analyzed to derive fundamental characteristics of the combustion concepts under investigation. It is worth noting that, due to the high turbulence levels, detection of the spray and flame with a threshold value often leads to errors. Therefore, the detection is based on a predefined probability density function dependent on the image zone (background, dense core, flame) to assign pixel values to a specific location. This allows the more precise identification of contours associated with quantities such as spray tip penetration and flame propagation.

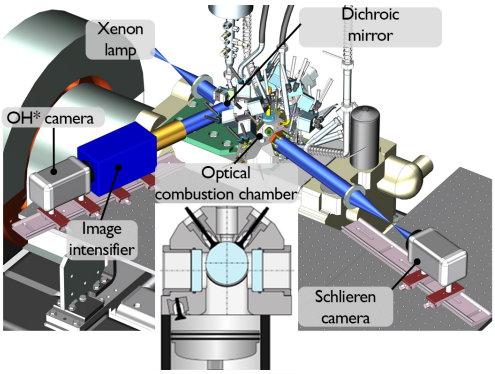

Figure 2. Optically accessible combustion chamber and setup for simultaneous high-speed Schlieren and OH* chemiluminescence measurements.

The determination of the effective start of injection (SOI) is based on the Schlieren spray contour which can be observed in steps of 0.1 deg CA throughout the relevant part of the process. For each step, the penetration of the pilot spray tip into the combustion chamber is determined from the correspondingly enhanced Schlieren image. The effective start of injection is then determined based on the temporal evolution of the spray tip position by extrapolating backward to zero penetration, thereby using the well-known [18,19] linear behavior during the initial injection phase, which is visualized in Figure 3. This is done to account for the fact that even the highest camera frame rates never facilitate a systematic capture of every actual injection begin, since it cannot be accurately timed due to the inherent slightly deviating hydraulic delay of the injector.

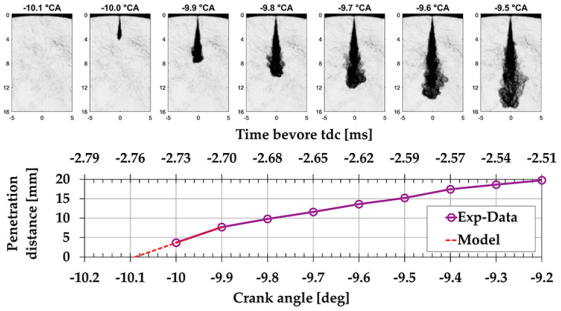

Figure 3. Effective SOI evaluation using optical imaging and linear model in between first images.

The OH* chemiluminescence measurement allows detecting ignition and represents an integrated line-of-sight signal along the entire measurement volume. Even though other species (e.g. CO*), particularly under lean conditions at high pressures, may contribute considerably to the overall chemiluminescence signal at progressing combustion [20], the first OH* chemiluminescence emission can always be clearly attributed to ignition [21]. Moreover, also the interference of soot incandescence does not (yet) affect the ignition detection [22], especially since the chosen combustion strategy using a small quantity of pilot fuel should not produce interfering quantities of soot. The start of (high temperature) combustion has been defined as the first OH* appearance, respectively the first image containing a “brighter spot” [23]. The automated optical ignition delay detection proved to be reliable, also compared to the corresponding ignition delay detection from the heat release analysis.

2.3 Exhaust gas extraction, conditioning and measurement

An experiment is constituted by multiple combustion cycles (typically 25). Sufficient preparation (two) and purging cycles (three) are run to achieve stable boundary conditions before and after each combustion cycle. Due to this process sequence, a fast-switching valve was developed for the exhaust gas analysis, which separates the exhaust generated during combustion cycles from the gas flow stemming from preparation/purge cycles. Figure 4 shows the corresponding division of the exhaust gas channel by this valve, whereby the exhaust gas from the combustion cycles to be analyzed is led into a conditioned system. A lateral moving control piston (marked in pale red in Figure 4) routes the individual exhaust gas pulses to either the conditioned system or the purge gas disposal system. The conditioned system consists of a cylindrical volume (5.1 l), allowing gas pressure dampening for the exhaust gas analyzing system. The damping volume provides enough exhaust gas for the time between the fired cycles (1.3s) and it can provide an additional extraction time of 12 s after the last experiment. The exhaust gas path as well as the gas dampening volume are heated to 196°C. Moreover, the exhaust gas sampling point distance from the exhaust valve is only around 500 mm to ensure a minimum of post reactions. Additionally, an exhaust gas temperature probe is located directly after the exhaust gas switching valve to ensure that only combustion cycles are measured. It consists of a 0.2 mm thermocouple embedded in a 1 mm fixation tube ensuring the safe protrusion of the thermocouple tip by 4 mm in the free stream for very fast response. The exhaust temperature is then evaluated on a cycle basis.

The exhaust gases are analyzed using a FTIR based measurement system (AVL SESAM i60 FT SII), which is equipped with a special evaluation method based on actual fuel such as gasoline, diesel, methanol, ethanol, ammonia, or for this particular study methane. This grants fast and exact exhaust gas evaluation in a wide range of CH_4 concentrations and simultaneous detection of other species.

2.4 Measurement procedure and analysis

Table 2 gives an overview of the operating settings of the measurements in terms of methane/air mixture charge conditions such as air-fuel equivalence ratio (λ) and boost pressure variation. Gas admission pressure, start and duration (based on initially determined injection rate characteristics according to energizing time ET) can be set independently by a separate fuel supply unit to accommodate the boost pressure variation.

Note that the compression temperature (T_c) and pressure (p_c) are based on pure air compression. These are denoted as reference values for all gas/air combustion investigations, as certain parameters, such as effective compression pressure and temperature, are dependent on the specific gas respectively mixture charge properties.

Table 2 Experimental conditions

$CH_4 + H_2$ / air mixture charge		
Air-fuel equivalence ratio λ	1.0 – 2.5 (0.25 steps)	
Pilot fuel	dodecane	[-]
Start of pilot injection (SOI)	-10	[°CA]
Injection pressure	1000	bar
ET / DOI	500 / 523	[µs]
Compression pressure p_c	70	[bar]
Start of gas admission	60° before IVO	[°CA]
Gas admission pressure	9	[bar]
Intake temperature T_{in}	50 / 100 / 150	[°C]
Compression temperature T_c	850 / 900 / 950	[K]

Start of ignition, ignition delay (location), combustion onset, and flame propagation have been evaluated by post-processing procedures of the simultaneous high-speed Schlieren and OH* chemiluminescence measurements. Combustion heat release rate has been analyzed by applying an in-house thermodynamic two-zone model that considers dissociation in the burnt gas zone and accounts for losses by wall heat transfer, piston ring blow-by, and crevice volumes [24]. Due to the unique test facility layout (optical combustion chamber vs. working cylinder), significant efforts were made in terms of high precision pressure acquisition [11]. The wall heat losses were estimated using an adapted Woschni approach (including extended heat transfer coefficient α_W based on flow measurements) Piston-ring blow-by was measured, and the volume of crevices was determined from the drawings. However, since the wall-heat loss model had to be tuned by distinctive constants, the results are denoted as apparent heat release rate (aHRR).

The ignition delay can be deduced from both optical data (OH* chemiluminescence) and from the calculated heat release rates. The heat release rate-based ignition detection has been thoroughly validated and shows a very good agreement with the optical data (already presented in [16]). The ignition delay calculation method is very sensitive and therefore allows detection of ignition at about 0.35% - 0.5% of the total heat released. In addition to the ignition delay, a transition time is calculated. The transition time is the time that passes between the ignition of the pilot fuel and the start of the combustion of the premixed charge. This time is calculated as the time delay between the start of the HRR and the time when the known energy contained in the pilot fuel is converted. This start of

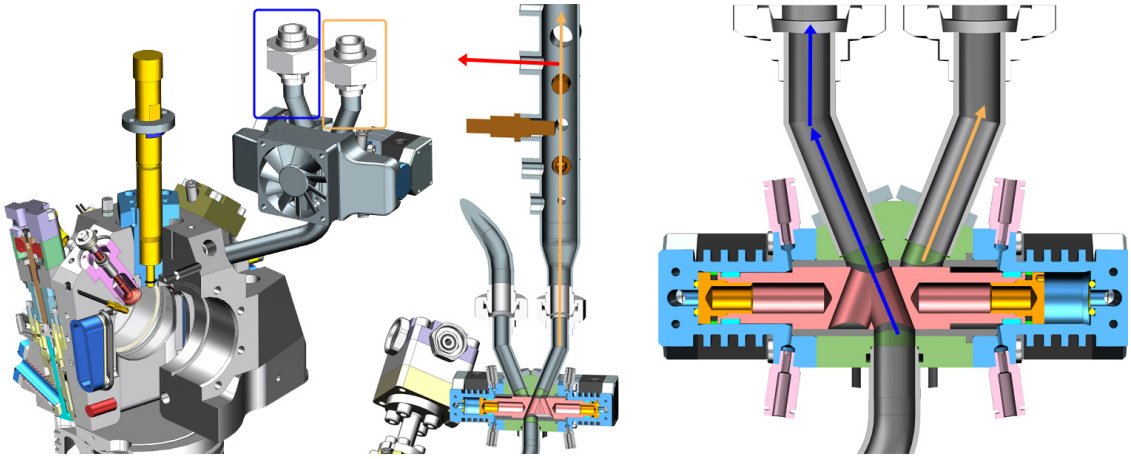

Figure 4. Exhaust gas path separation by a fast-switching valve (full assembly left, cross-section right), and conditioned exhaust gas sampling section (including sensors) in front of the exhaust gas storage system (center). Marked sampling point (red arrow), cold air separation (blue arrow) and combustion cycle exhaust gas extraction (amber arrow).

main charge combustion is calculated based on the known pilot fuel energy and is set just above the theoretical heat release of the pilot fuel jet.

An apparent flame propagation speed (s_{aFP}) can be determined from the Schlieren measurements, respectively the contour displacement representing the flame surface. The method applied here consists of a two-dimensional spatially averaged evaluation of reaction zone expansion based on the optical measurements. It resolves local behavior very well (i.e. large propagation speeds) but is also prone to misidentification of burned zones, since it still contains uncertainty in differentiation of the cause of refractive index variations. In addition, the effect of flame compression and expansion cannot be corrected for pressure variations, and the determined s_{aFP} always includes the effect of the expanding burned zone. Thus, higher pressure ratios are affecting the resulting s_{aFP} stronger for lower air-fuel equivalence ratios. However, the chosen approach can deal with (local) transport phenomena and allows a reasonably accurate evaluation during the early combustion phase. The designation ”apparent” shall point out that the analyzed flame propagation speed must be interpreted as a qualitative value that nevertheless enables a comparison within operating parameter variations.

The properties of hydrogen as fuel are compared to methane as standard fuel (as well as the pilot fuel dodecane) in Table 3 to illustrate the large discrepancies in terms of AFR, LHV and flame speed. The high flame speed of hydrogen means that much faster combustion progress can be expected, which may need adjustments of relevant control parameters. The slightly lower auto-ignition temperature and very low ignition energy suggest that higher hydrogen concentrations might result in abnormal combustion (pre-ignition and knocking). The slightly lower heating value per volume requires higher volumetric fuel flow rates to maintain the in-cylinder energy. The stoichiometric air amount changes as well and increases with higher

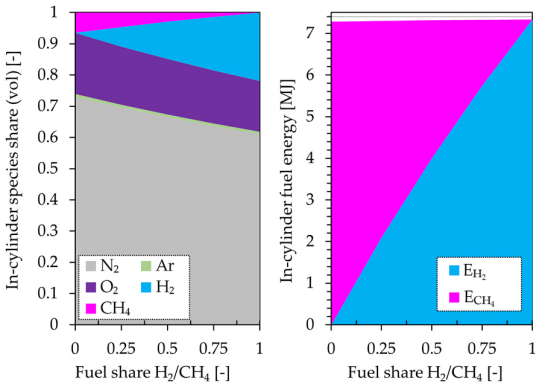

Figure 5. In-cylinder species share for a CH_4/H_2 variation exemplarily for λ = 1.5 and constant volumetric cylinder charge (left) and in cylinder fuel energy for the same conditions (right).

hydrogen concentrations. Since the experiments are performed at specific air-fuel equivalence ratio levels, this effect is partially compensated, leading to a reduced air amount for rising H_2 fractions and marginally increasing the total in-cylinder energy. Figure 5 summarizes the effects described in terms of in-cylinder species share resp. fuel energy according to H_2/CH_4 fuel share.

3 RESULTS

The work presented is based on results of methane dual-fuel combustion investigations reported earlier [11, 12]. Following a brief introduction of pilot fuel ignited hydrogen enriched methane combustion, the impact on characteristic quantities such as ignition delay and emissions is assessed for variations of key operational parameters. Heat release analysis is used for that purpose, complemented by selected high-speed imaging data. The following results are given in groups of fuel-shares and temperature levels, where the denoted 10%, 20% and 30% H_2 are always volume fractions while the 50°C, 100°C and 150°C are the intake temperature conditions.

Table 3 Properties of dodecane $C_{12}H_{26}$ (pilot), compressed hydrogen (H_2) and methane (CH_4) [25-27].

	Storage conditions	Density @ storage conditions	LHV @ storage conditions	Flammability limits in air	Stoichiometric AFR (mass)	LHV per Vol. @ stoichiometry (0.1 MPa, 373 K)	Auto-ignition temperature	Minimum ignition energy	LBV @ stoichiometry (0.1 MPa, 300 K)	RON
		[kg/m³]		*[Vol-%]*	*[-]*	*[MJ/m³]*	*[K]*	*[mJ]*	*[m/s]*	*[-]*
$C_{12}H_{26}$	0.1 MPa / 300 K	750	45 MJ/kg 33 GJ/m³	0.6 –7.5	14.9 : 1	–	480	~0.23	~ 0.8	–
H_2	70 MPa 300 K	39	120 MJ/kg 4.7 GJ/m³	4.7 – 75	34.3 : 1	~ 2.30	773 – 850	~ 0.016	3.5	> 100
CH_4	25 MPa 300 K	187	50 MJ/kg 9.4 GJ/m³	5 – 15	17.2 : 1	~ 2.45	860	~ 0.21	0.38	120

3.1 Combustion characterization

Figure 6 shows indicated mean effective pressure (p_{mi}) results for three different temperatures, four different hydrogen concentrations, and a variation of λ in the range of 1 to 2.5, in steps of 0.25. Varying temperature exerts a major influence, whereas the hydrogen concentration variation shows a large impact only at very lean conditions above 2.2. For all experiments, the charge air pressure has been kept constant, leading to a similar volumetric cylinder charge but a reduced in-cylinder mass for higher intake temperatures due to lower density, which in turn results in a lower p_{mi}.

The lean conditions for the coldest temperature setting suffer from poor combustion and therefore result in clearly decreased p_{mi} over higher temperature settings. The regions with poor combustion can be better identified when considering the coefficient of variation of p_{mi} (COV) given in Figure 7. Hereby, the lowest level in COV can be seen around λ = 1.75. The fuel richer conditions are having a reproduceable start of combustion, but in later combustion phases partial knocking can be detected, which increases the COV. The higher intake temperature also leads to higher COV due to partial knocking at fuel rich conditions. On the other hand, it contributes to smaller COV at very lean conditions due to the lower occurrence of poorly burning cycles (near misfiring), maintaining a steady flame propagation in early combustion phases due to higher reaction rates.

The hydrogen addition reduces COV for cold conditions in a wide range and especially for lean mixture compositions. For example, the COV is three times smaller (2% instead of 6%) for λ = 2 at Tin = 50°C. For hotter conditions at 100°C, the influence of hydrogen addition does not reduce the

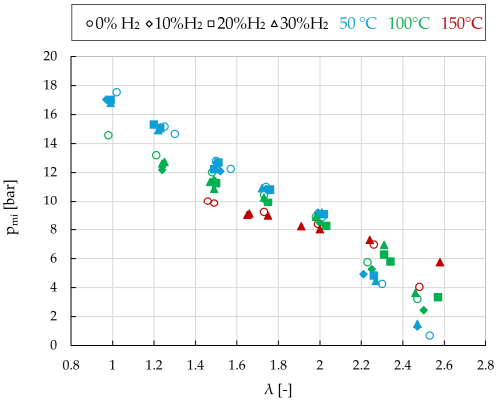

Figure 6. Indicated mean effective pressure in dependence of 4 different hydrogen concentrations in relation to three different intake temperatures covering the examined operating range.

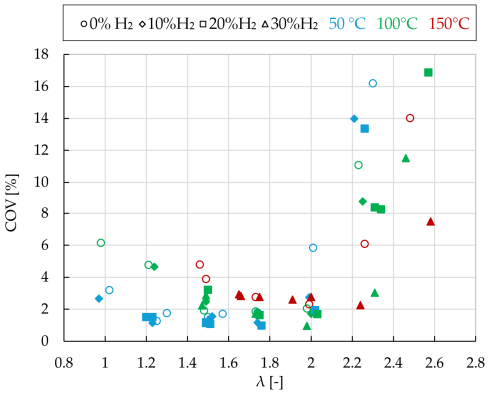

Figure 7. COV in dependence of 4 different hydrogen concentrations in relation to three different intake temperatures

COV drastically below λ = 2 but it improves combustion stability above λ = 2 where COV is reduced up to 5 times. Hereby hydrogen can reduce the ignition delay leading to an earlier flame propagation and increased flame speed leading to an overall shorter burn duration. The earlier combustion at higher temperatures is therefore more stable, resulting in a lower COV. This will be later confirmed in Figure 11.

Looking at the variation of the hydrogen content at constant intake temperature, the almost subliminal influence of the hydrogen addition can be recognized in the cylinder pressure curves. Figure 8 shows the mean cylinder pressure (p_{cyl}) from 25 experiments for three different λ and four hydrogen concentrations. Under stoichiometric conditions, the main influence of hydrogen was observed at hydrogen concentrations of 10%, resulting in a noticeable increase in cylinder pressure of around 7 bar. Most likely, this influence is due to the higher flame speed, which leads to faster combustion. The case at λ = 1.5 shows the highest cylinder pressure for 30% H_2. An increase in combustion pressure can be observed later in the combustion process at around 15 deg, but an earlier increase in combustion-related cylinder pressure can be seen too. The effects of hydrogen addition on the different combustion phases can be better understood when evaluating the apparent heat release rates shown in Figure 9.

In the beginning, the flame can expand freely around the pilot in the optically accessible combustion chamber. Subsequently, when it reaches the bottom of the chamber, it propagates down through the narrow connection to the engine cylinder to consume the charge there.

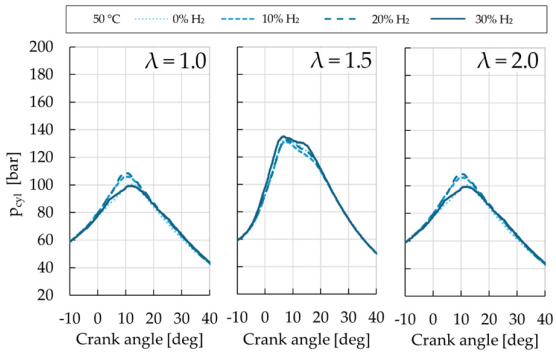

Figure 8. Cylinder pressure for three different air-fuel equivalence ratios at an intake temperature of 50°C for 0%, 10%, 20% and 30 %H_2 concentration.

The separate combustion process leads to this two-stage combustion as described before. Due to this specific combustion characteristic of the Flex-OeCoS, IC engine typical values describing the burning behavior in later combustion phases, such as burned mass fraction at 90% (MBF90), should not be compared to real engine measurements.

The ignition and early combustion process detectable in the apparent heat release rate in Figure 9 top appears to be very comparable for all hydrogen concentrations. Even the temperature rise from 50°C to 100°C seems to have minor impact since the heat release rate reaches about 400 J/deg at TDC for either case. The ignition delay of the injected dodecane (SOI = -10 deg) is quite similar for all hydrogen variations but in the more detailed view (bottom row), the expectable difference in ignition delay for the higher temperature can be already seen since the 100°C tends to have the combustion started about 0.5 deg earlier.

A distinctive heat release peak can be detected due to the pilot fuel combustion followed by a little “dip” (visible in the bottom subplots in Figure 9) before the premixed combustion starts. The height of the aHRR of the pilot combustion might be influenced by the heat capacity of hydrogen since more energy is needed to preheat the charge until the mixture starts to react and contribute to the combustion. For the higher temperature, the aHRR of the pilot charge is significantly lower, which might be in contrast to the expected higher reaction rate. Since the ignition delay is slightly lower at higher temperatures, the time for the expansion of the pilot jet is lowered. Therefore, the local fuel concentration is higher, leading to a fuel richer mixture, which lowers the flame speed. Additionally, the reactive surface is smaller since the pilot jet plume is less voluminous, thus contributing to the lower heat release rate. Only the case with the highest hydrogen concentration shows a lower ignition delay and higher aHRR. The higher temperature leads to sufficient ignition energy, which might promote thermal decomposition of the premixed fuel in the flame-near zones, followed by oxidation, contributing to the overall heat release of the pilot fuel. The earlier start of ignition leads to a slightly earlier main combustion and a very high heat release in the second combustion phase, which was close to knocking. The hottest experiment setting was therefore aborted because the main fuel charge burned under knocking conditions.

Figure 10 provides a comparison of the cumulative heat release data obtained in the experiments at 50 and 100°C at air-fuel equivalence ratios of 1,0, 1.5 and 2.0, for all levels of H_2 addition. To this end, the individual data have been normalized with the respective overall fuel energy input, additionally taking into account the results from the emission measurements in order to determine the actual fuel conversion rate.

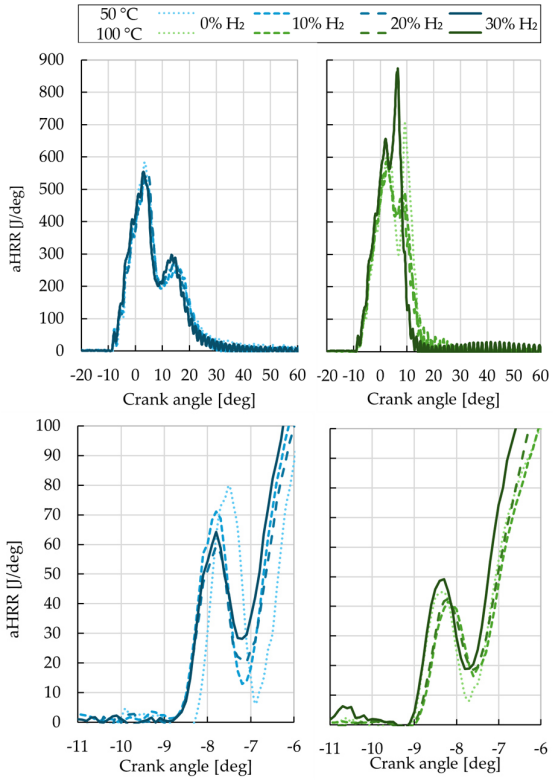

Figure 9. Apparent heat release rate at λ = 1.5 for four different hydrogen concentrations and two different intake temperatures (top row: complete combustion duration, bottom row: zoom-in on initial phase, left: 50°C, right: 100°C)

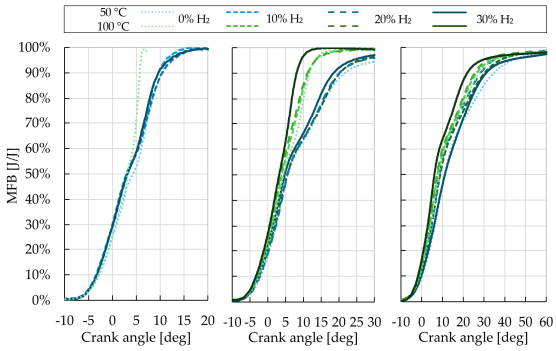

Figure 10. Burned mass fraction histories for three different air-fuel equivalence ratios (λ = 1.0, 1.5 and 2.0 left to right) at intake temperature of 50°C and 100°C for 0%, 10%, 20% and 30% H_2 concentration

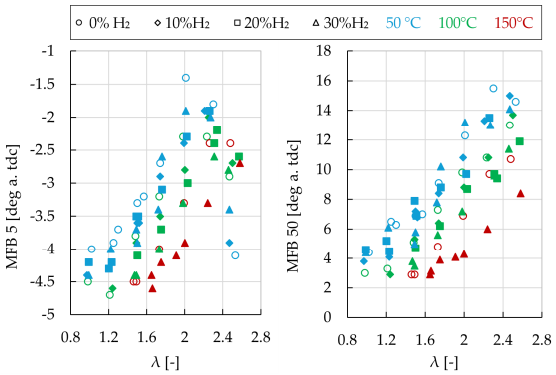

Figure 11. Timing of 5% (Left) and 50% (right) mass fraction burnt for all experiments derived from the apparent heat release calculation.

The overall fuel conversion rate was quite high for all experiments resulting in a range of 98.3 to 99.6%. The remaining unburned fuel was most likely trapped in the large crevice volumes of the Flex-OeCoS due to e.g. many window and insert seals. The overall faster heat release at higher temperatures at λ = 1.0 and 1.5 can be confirmed. For the lean case at λ = 2.0 the higher hydrogen content of 30% contributes especially for the higher temperatures, while, at lower temperatures, a small share of hydrogen (10%) already reduces the burn duration leading to earlier high cumulative heat release.

From the burned mass fraction evolutions, the characteristic numbers MFB5 and MFB50 can be derived, which allow easier comparison of flame onset and combustion duration (see Figure 11). The MFB5 and MFB50 are reached much earlier for the hotter conditions and might be more influenced by temperature than hydrogen substitution.

But the MFB characteristic numbers are clearly affected by hydrogen addition. For example, the λ = 1.5 case shows that 30% H_2 substitution has the shortest MFB5 and is close to MFB5 for 0% H_2 at 50°C higher intake temperature. MFB50 shows mixed results: At 100°C the MFB50 is reached earlier throughout the air-fuel equivalence range if hydrogen is present. In contrast, at the lower temperatures, specifically at 50°C, the effect is less clear and very λ-dependent.

The more detailed analysis of the high-speed image data facilitates an easier understanding of the phenomena involved in the hydrogen variation such as shown in Figure 12. The superimposed magenta colorized OH*-Chemiluminescence high speed imaging over the Schlieren imaging serves as a perfect basis to identify spray penetration, evaporation, onset of the initial flame and later flame propagation. The overview images shown in Figure 12 are used to determine combustion characteristics such as aHRR, whereas the higher resolved images as shown in Figure 14 below can be used to optically identify the ignition delay.

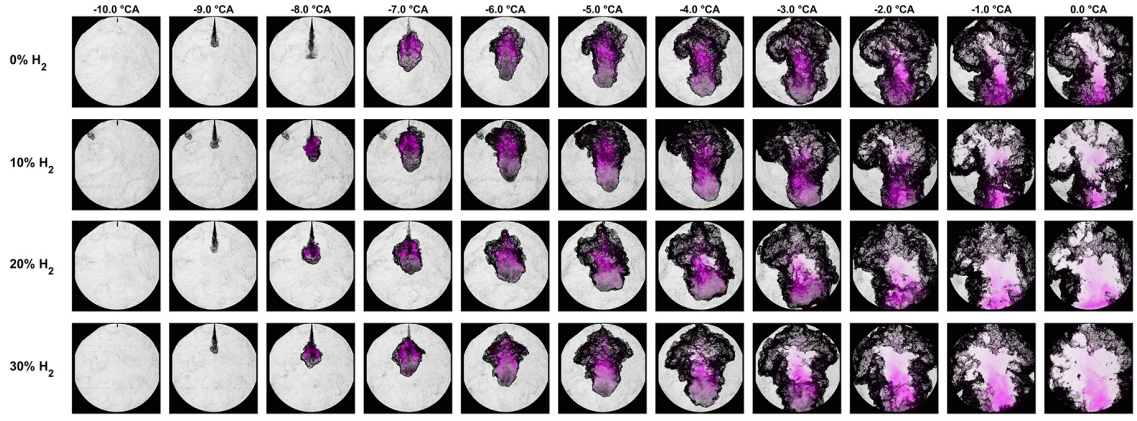

Figure 12. Optical image superposition of OH* (magenta) and Schlieren imaging at intake temperature of 50°C, SOI = -10 deg CA and for 0%, 10%, 20% and 30% H_2 concentration.

As could be seen already in Figure 9 when zooming in on the initial combustion phase, at 50°C the addition of hydrogen has a direct impact on ignition delay. The pure methane case clearly shows a later start of combustion, whereas ignition delay seems to be largely insensitive to the level of hydrogen concentration. This behavior is also reflected in the optical data shown in Figure 12. The propagation speed of the flame derived from the Schlieren flame contour can be assumed to be slightly lower for the pure methane case and is increasing with hydrogen concentration. This can be seen when focusing on the range between -2.0 and 0.0 deg CA and giving particular attention to the unburned zone.

The ignition delay derived from the optical measurement is in good consistency with the thermodynamic identification, hence only one ignition delay is given in Figure 13. In addition to the ignition delay, the transition time is shown. Whereas the longer ignition delay for the 0% H_2 case was already detectable in Figure 12, the ignition delay for the H_2 variation is very close together, therefore a more detailed insight into the optical results is given in Figure 14. Basically, at 50°C, the 10% H_2 case shows the smallest ignition delay for averaged cycles (based on Figure 13), but based on median cycles shown in Figure 14, the ignition delay was substantially lower with increasing H_2 amounts. This deviation comes from single combustions with a comparable low ignition delay, lowering the average value below the median.

For the hotter cases, the pure methane cases seem to have the shortest ignition delay. This can be explained as a consequence of the high heat capacity of hydrogen, which leads to colder in-cylinder temperatures during compression with increasing amounts of hydrogen at constant intake temperature, and since the compression temperature is already high enough with T_{in} = 100°C, the combustion starts earlier even without hydrogen addition.

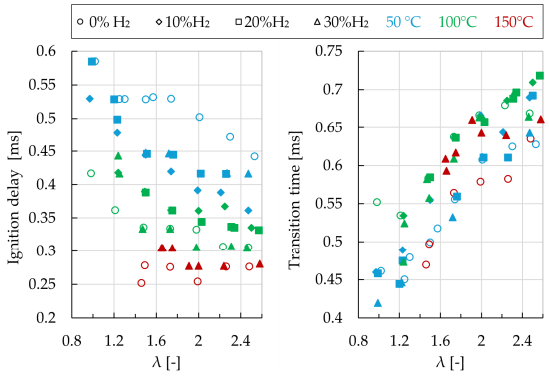

Figure 13. Ignition delay (left) and transition time (right) for all conducted experiments.

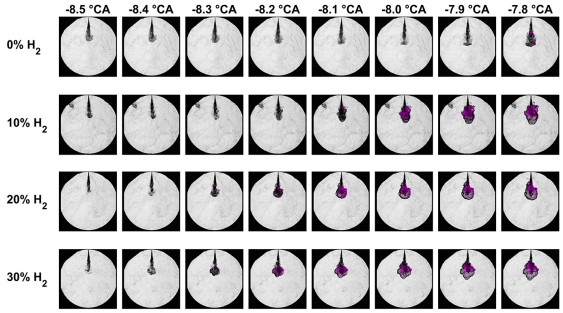

Figure 14. Detailed insight into pilot spray propagation, ignition and flame evolution within the combustion chamber at intake temperature of 50°C, SOI = -10 deg CA and for 0%, 10%, 20% and 30% H_2 concentration by means of Schlieren overlayed OH*-chemiluminescence images at high temporal resolution.

The transition time constantly increases over λ, which is according to expectations. Since the ignition delay decreases with increasing λ, the in-cylinder conditions outside of the initial flame front are colder at start of combustion in the main charge and less energy is released by the pilot combustion. This is due to the fact that a small portion of the premixed charge is always burned together with the pilot fuel combustion, increasing the heat release of the pilot charge with λ close to 1.0. The transition time over the hydrogen variation remains largely constant for the 50 and 100°C cases whereas the 150°C case shows an increased ignition delay as well as transition time for the higher H_2 amount.

The apparent flame propagation speed derived from the optical imaging is shown in Figure 15 and describes the growth of the line-of-sight integrated flame spread based on the Schlieren imaging. The flame speed given can then be separated into two different regions, the flame speed during the pilot fuel combustion between -10 and -9 deg and the flame speed during the later main charge combustion. The calculated flame speed is only valid before the flame touches the wall, therefore a limited window between start of combustion and -1 deg is given in Figure 15.

For the main combustion phase the flame speed is generally increased due to hydrogen addition supporting the increased reactivity thesis. For the 50°C and 100°C case the highest H_2 concentrations show the overall highest flame speed and therefore fulfil the expectation: Based on single species properties (see Table 3), hydrogen has a much higher laminar flame speed and hence it can be expected that the turbulent flame speed for any mixture of methane and hydrogen will also be higher than with pure methane.

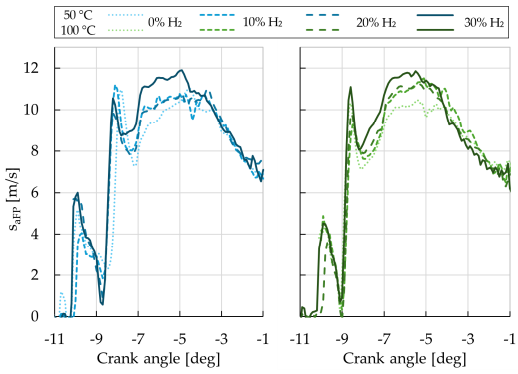

Figure 15. Calculated apparent propagation flame speed from Schlieren imaging for 50°C (left) and 100°C (right) intake temperature at λ = 1.5 for four different H_2-concentrations

The pilot flame speed is largely unaffected by hydrogen concentration. Only the 10% case for the colder conditions and the 20% case for the hotter conditions lead to a slightly delayed rise and smaller maximum flame speed. Generally, it is expected that the pilot related flame speed is only marginally influenced by the hydrogen quantity since the inner core of the pilot jet plume mostly consists of dodecane with constant fuel properties.

3.2 Emissions

Even though great efforts have been made to make the gas extraction as constant and reproducible as possible, it must be emphasized once again that emissions from the Flex-OeCoS are deviating from those of actual engines, for a variety of reasons: On the one hand, emissions formation processes are affected quite significantly by the distinct two-stage combustion process described above. On the other hand, the combustion chamber has larger crevice volumes as well as a larger surface to volume ratio than any engine, which inevitably leads to higher emissions of unburned fuel. Therefore, no absolute emissions data are presented in the following, but all results are normalized to the respective levels at a reference condition (intake temperature 50°C, air-fuel equivalence ratio of λ = 1.5, without hydrogen addition). It can be expected that trends can be identified on that basis which may also be relevant for engine applications.

Since hydrogen enriched methane combustion is considered a viable option for reducing GHG emissions, it is very important to assess its effectiveness in terms of reducing CO_2 emissions as well as contributions from other greenhouse gases, specifically methane slip (CH_4). However, emissions of pollutants such as carbon monoxide (CO) and nitric oxide (NO_X) must also be kept under control. Therefore, results for all these components are shown in the following, typically as power specific, normalized values.

Normalized CO_2 emission data are shown in Figure 16. For all levels of intake temperature, in the pure methane case, a characteristic with a clear minimum can be observed. This minimum is shifted towards higher air-fuel equivalence ratio with increasing temperature and the overall behavior is obviously reflecting the fuel efficiency characteristic. The coldest conditions show an overall lowest specific CO_2 output and the influence of H_2 can easily be detected. An addition of 30% (per volume) H_2 (6% energy) to the λ = 1.5 point hereby leads to an overall reduction of 8.6% CO_2. However, the results are not very consistent in terms of the CO_2 reduction potential: At the same intake temperature, the emissions levels are almost indiscernible for any intermediate H_2 addition levels. The 100°C values are scattered around the baseline curve and the benefit of hydrogen addition can only be detected for the highest air-fuel equivalence ratios. At the highest intake temperature, the benefit of 30% H_2 again seems to be in the same range as for the lowest one. It is therefore difficult to draw final conclusions, but there are indications that a reduction of CO_2 emissions in the range of the energy content (6% - 7%) of the added hydrogen is within reach, especially for the coldest conditions.

Figure 17 shows the trend of methane emissions as a function of air-fuel equivalence ratio for the same range of conditions. In contrast to the other diagrams in this chapter, the data depicted here are not only normalized to the reference condition values, but the specific emissions calculated in the first step are then referenced to the gas fuel consumption of the respective case before

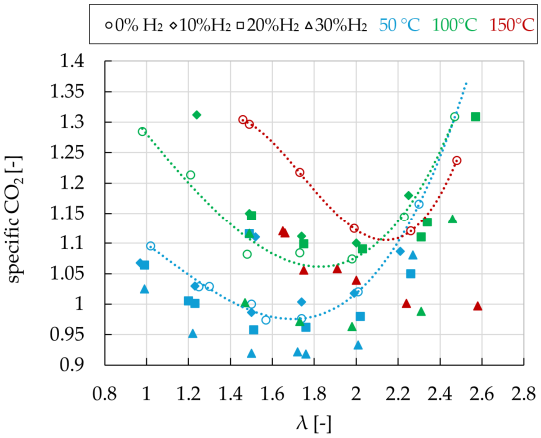

Figure 16. Normalized specific CO_2 emission, covering the broad range of operating conditions in terms of air-fuel equivalence ratio, intake temperature and hydrogen addition.

normalization. According to earlier investigations at large engine conditions, the relative emissions of CH_4 are strongly correlated with the effect of quenching and hence the thickness of the quenching layer [28]. The almost linear characteristic as a function of air-fuel equivalence ratio in the logarithmic plot shown in Figure 17, as well as the (moderate) sensitivity to variations of temperature are well in line with what can be expected on this basis. Despite the evident scatter in the data, there seems to be a clear tendency towards reduced methane slip with increasing hydrogen addition – in some cases, reductions from the pure methane case by factors of almost two are observed. From first principles, it would appear realistic that this reduction is in the range of the volumetric share of the hydrogen in the fuel mix, an assumption that the present data can be considered largely in line with.

Specific CO and NO_X emissions are shown in Figure 18. As to be expected, carbon monoxide emissions are increasing towards lean conditions and lower temperatures. Hydrogen addition not only reduces the carbon content in the fuel mix but also promotes faster and more complete combustion, as we have seen in Figure 9 and Figure 10. Therefore, the positive effect of increasing the share of hydrogen in the fuel mix in terms of lower CO emissions is in line with expectations.

NO_X emissions show the well-known trend over air-fuel equivalence ratio, with a pronounced peak at $\lambda = 1.25$. Towards lean conditions, a nearly linear reduction can be seen in the logarithmic diagram; NO_X emissions are decreasing about an order of magnitude when reducing λ by 0.5. Increasing temperature is known to enhance NO_X formation and emission levels are increased accordingly.

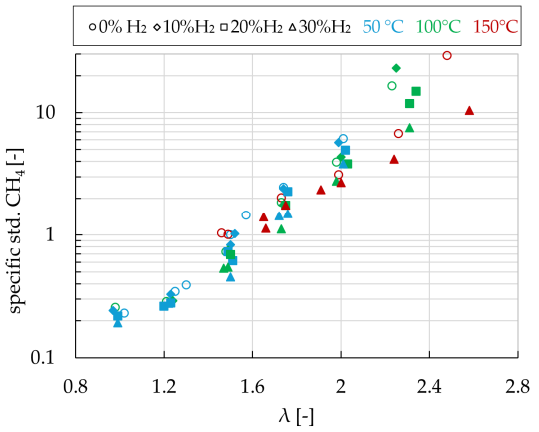

Figure 17. Normalized specific CH_4 slip, covering the broad range of operating conditions in terms of air-fuel equivalence ratio, intake temperature and hydrogen addition.

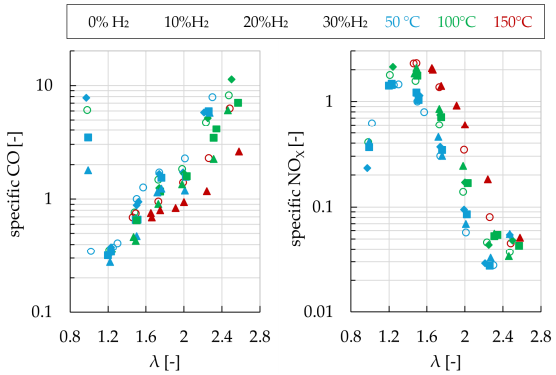

Figure 18. Normalized specific emissions of CO (left) and NO_X (right) covering the broad range of operating conditions in terms of air-fuel equivalence ratio, intake temperature and hydrogen addition.

Hydrogen addition slightly increases NO_X emissions, which is in line with the trend wise faster combustion with increased hydrogen content, which can be expected to promote the formation of nitric oxide by increasing the share of the volume with favorable conditions (high temperature, long residence time).

4 CONCLUSIONS

Hydrogen enriched methane combustion initiated by a pilot fuel spray has been characterized in the optically accessible Flex-OeCoS test facility for a variation of air-fuel equivalence ratios, intake temperatures and hydrogen concentrations. This included, besides the acquisition of highly resolved thermodynamic data and simultaneous high-speed Schlieren and OH* chemiluminescence measurements, the determination of exhaust emissions. For this purpose, the test facility has been extended to allow the separation of exhaust gas from the different phases in its aperiodic operation as well as the proper measurement of emissions from the relevant combustion cycles. The variation of both temperature and air-fuel equivalence ratio allowed covering a wide range of loads (p_{mi}). The data obtained has been analyzed to determine key parameters such as ignition delay, heat release (rate), COV and specific emissions of greenhouse gases as well as pollutants. Moreover, more detailed combustion characteristics such as the apparent flame propagation speed have been analyzed.

In general, combustion stability seems to be enhanced by the addition of hydrogen. The general characteristic of COV as a function of air-fuel equivalence ratio remains largely unaffected. Lowest levels are observed around $\lambda = 1.5$, with slight increase towards richer mixtures. This is due to partial knocking in the late combustion phase and in-

creasing instability at leaner conditions as consequence of the more frequent occurrence of poorly burning cycles (near misfiring). The stabilizing effect can be attributed to the impact of hydrogen addition on both ignition delay and apparent flame speed – even though there are counteracting phenomena: On the one hand, the lower ignition energy of hydrogen vs methane tends to reduce the time until ignition takes place. On the other hand, the higher heat capacity of hydrogen compared to methane leads to lower temperatures after compression and requires more energy to preheat the charge until hydrogen starts to contribute to the combustion reaction. At low intake temperatures, hydrogen addition resulted in a slightly shortened ignition delay, whereas, for increased temperatures, the effect was less pronounced or even inversed. As regards the apparent flame propagation speed, however, the addition of hydrogen always leads to accelerated flame growth, which results in corresponding faster and more stable combustion characteristics

The emissions measurements confirm that there is a potential for hydrogen enriched methane to reduce GHG emissions; however, the results are far from conclusive and the effect must be considered rather moderate: As regards the reduction of CO_2, it is at best in the range of the energy share of hydrogen in the fuel mix; hence, for the up to 30% per volume replacement of methane, it does by no means exceed the single digit percentage range. The benefit in terms of methane slip may be more pronounced and achieve percentage levels up to the volumetric share of hydrogen in the fuel mix. The trends with respect to emissions of pollutants are conforming with expectations and appear to be the logical consequence of the impact of hydrogen addition on combustion characteristics: Carbon monoxide emissions tend to decrease with increasing share of hydrogen, whereas nitric oxide emissions are increased.

The results obtained in the present investigation provide important insight as regards the applicability of hydrogen enrichment for gas-fueled engines; however, observations made on the Flex-OeCoS cannot be directly transferred to large engines. In a next step, extensive simulations performed by means of properly validated tools have to be performed for identifying the to be expected impact of hydrogen addition on a large dual-fuel engine and any resulting adjustment needs. This will then serve as a basis for confirmation of the potential in first engine tests.

5 DEFINITIONS, ACRONYMS, ABBREVIATIONS

aHRR: Apparent heat release rate
aHR: Apparent heat release
AFR: Air-fuel ratio
CA: Crank angle
COC: Center of combustion
COV: Coefficient of variability
DOI: Duration of injection
DF: Dual fuel
GHG: Greenhouse gas
ID: Ignition delay
LHV: Lower heating value
MFB: Burned mass fraction/mass fraction burnt
MFB5: Timing of 5% mass fraction burnt
MFB50: Timing of 50% mass fraction burnt
$\mathbf{p_{cyl}}$: Cylinder pressure
$\mathbf{p_{mi}}$: Indicated mean effective pressure
PIV: Particle Image Velocimetry
RJ: Reactive jet
$\mathbf{s_{aFP}}$: apparent flame propagation speed
SOI: Start of injection
STD: Standard deviation
TDC: Top dead center

6 ACKNOWLEDGMENTS

Financial support from the Swiss Federal Office of Energy (SFOE, contract SI/502152-01) as well as funding by WinGD Ltd. is gratefully acknowledged.

7 REFERENCES AND BIBLIOGRAPHY

[1] P.R. Shukla, J. Skea, R. Slade, A. Al Khourdajie, R. van Diemen, D. McCollum, M. Pathak, S. Some, P. Vyas, R. Fradera, M. Belkacemi, A. Hasija, G. Lisboa, S. Luz, J. Malley, (eds.). IPCC, Climate Change 2022: Mitigation of Climate Change. Contribution of Working Group III to the Sixth Assessment *Report of the Intergovernmental Panel on Climate Change* [Cambridge University Press, Cambridge, UK and New York, NY, USA. ISBN 978-92-9169-160-9.

[2] International Maritime Organization, *Resolution MEPC.377(80) – 2023 IMO Strategy on Reduction of GHG Emissions from Ships*

[3] DNV. 2020. Maritime Forecast to 2050. *Energy Transition Outlook 2020 (Det Norske Veritas).*

[4] Abbasov F., Calvo Ambel C., Hemmings B. and Gilliam L. 2018. Roadmap to decarbonising European shipping. *T&E - Transport & Environment.*

[5] Ash N. and Scarbrough T. 2019. Sailing on Solar – Could green ammonia decarbonise international shipping?. *Environmental Defense Fund*. 2019.

[6] Lloyd's Register, UMAS (2019a). 2019. Fuel production cost estimates and assumptions. *Lloyd's Register; UMAS*

[7] Lloyd's Register, UMAS (2019b). 2019 Zero-Emission Vessels: Transition pathways. Low Carbon Pathways 2050 series. *Lloyd's Register; UMAS*

[8] Lloyd's Register UMAS (2020). 2020. Techno-economic assessment of zero-carbon fuels. *Lloyd's Register; UMAS*

[9] Osterkamp P., Smith T., Søgaard K. 2021. Five percent zero emission fuels by 2030 needed for Paris-aligned shipping decarbonization. *Global Maritime Forum. Getting to Zero Coalition (ed.)*

[10] Schneider B., Schürch C., Boulouchos K., Herzig S., Hangartner M., Humair D., Wüthrich S., Gossweiler C. and Herrmann K.2020. The Flex-Oe-CoS – a Novel Optically Accessible Test Rig for the Investigation of Advanced Combustion Processes under Engine-Like Conditions, *Energies*. 13(7). 1794. https://doi.org/10.3390/en13071794.

[11] Wüthrich S., Humair D., Herrmann K., Bertola A. 2020 Enhanced instrumentation of an optical research engine with unique combustion chamber. *14th Int. AVL Symposium on Propulsion Diagnostics, Baden-Baden*. ISBN 978-3-9816971-6-2.

[12] Humair D., Cartier P., Süess P., Wüthrich S., Herrmann K., Barro C., Schneider B., Schürch C. and Boulouchos K. 2020. Characterization of dual-fuel combustion processes, *Rostock 6th Large Engine Symposium*. ISBN 978-3-941554-22-1.

[13] Vera-Tudela W., Schneider B., Wüthrich S. and Herrmann K. 2021.Study on the ignitability of a high-pressure direct-injected methane jet using a diesel pilot, a glow-plug and a prechamber. *IJER-21-0139*.
https://doi.org/10.1177/14680874211048144.

[14] Vera-Tudela W., Schneider B., Wüthrich S. and Herrmann K. 2022. Study on the ignitability of a high-pressure direct-injected methane jet using a scavenged pre-chamber under a wide range of conditions. *IJER-1-14*.
https://doi.org/10.1177/14680874221093144.

[15] Wüthrich S., Cartier P., Süess P., Schneider B., Obrecht P. and Herrmann K. 2022 Optical investigation and thermodynamic analysis of premixed ammonia dual-fuel combustion initiated by dodecane pilot fuel. *Fuel Communications* 12. https://doi.org/10.1016/j.jfueco.2022.100074.

[16] Wüthrich S., Albrecht P., Cartier P., Herrmann K., 2022. Comparison of pilot fuel ignited premixed ammonia versus methane dual-fuel combustion. *The Future of Large Engines VII – Novel Technology and Fuel Options: The Route to Clean Shipping, 7th Large Engine Symposium*, Rostock, ISBN 978-3-941554-25-2.

[17] Wüthrich S., Albrecht P., Cartier P., and Herrmann K. 2024. The GHG reduction potential of high-IMEP pure ammonia combustion. *8th Rostock Large Engine Symposium 2024: The Future of Large Engines VIII*: Technology Concepts and Fuel Options: The Route to Clean Shipping. 293-318. https://doi.org/10.18453/rosdok_id00004647

[18] Schneider B., 2003, Diss. ETH Nr. 15004 "Experimentelle untersuchung zur spraystruktur in transienten, verdampfenden und nicht verdampfenden brennstroffstrahlen unter hochdruck", ETHZ, 2003. https://doi.org/10.3929/ethz-a-004522641.

[19] Von Rotz B., Herrmann K., Boulouchos K., 2015 "Experimental investigation on the characteristics of sprays representative for large 2-stroke marine diesel engines combustion systems", SAE 2015-01-1825.
https://doi.org/10.3929/ethz-a-010836986.

[20] Desantes J.M., García-Oliver J.M., Vera-Tudela W., López-Pintor D., Schneider B., Boulouchos K., "Study of the auto-ignition phenomenon of PRFs under HCCI conditions in a RCEM by means of spectroscopy", *Applied Energy*, Vol. 179, pp. 389-400, 2016. https://doi.org/10.1016/j.apenergy.2016.06.134.

[21] Srna A., Bolla M., Wright Y.W., Herrmann K., Bombach R., Pandurangi S.S., Boulouchos K., Bruneaux G., "Ignition characteristics of n-dodecane pilot fuel spray in a premixed compressed methane/air charge". *Proceedings of the Combustion Institute 37* (2019) 4741–4749. https://doi.org/10.1016/j.proci.2018.06.177.

[22] Desantes J.M., Pastor J.V., García-Oliver J.M., Vera-Tudela W., "An experimental study of the effects of fuel properties on reactive spray evolution using Primary Reference Fuels", *Fuel*, Vol. 163, pp. 260-270, 2016. https://doi.org/10.1016/j.fuel.2015.09.064.

[23] Srna A., Bombach R., Herrmann K., Bruneaux G., "Characterization of the spectral signature of dual-fuel combustion luminosity: implications for evaluation of natural luminosity imaging", *Applied Physics B* (2019) 125:120. https://doi.org/10.1007/s00340-019-7222-z.

[24] Obrecht P., 2021, "WEG: calculation of the heat development law based on measured combustion chamber pressure traces", in-house thermodynamic model, ETHZ-LAV & FHWN-ITFE.

[25] Lhuillier C., Brequigny P., Contino F., and Mounaïm-Rousselle C., 2020, "Experimental study on ammonia/hydrogen/air combustion in spark ignition engine conditions", *Fuel, vol. 269, no. February*, p. 117448. https://doi.org/10.1016/j.fuel.2020.117448

[26] McAllister S., Chen J.-Y., and Fernandez-Pello A. C., 2011, "*Fundamentals of Combustion Processes: Appendix*", Springer, New York, NY, USA.

[27] Frankl, S., Gleis, S., Karmann, S., Prager, M. and Wachtmeister, G., 2020. Investigation of ammonia and hydrogen as CO2-free fuels for heavy duty engines using a high pressure dual fuel combustion process. *International Journal Of Engine Research*, *22*(10), 3196–3208. https://doi.org/10.1177/1468087420967873

[28] Weisser, G., Nylund, I., Schneiter, D., "Greenhouse Gas (GHG) Emissions from LNG Engines, Review of the Two-Stroke Engine Emission Footprint", CIMAC 2019.

8 CONTACT

Silas Wüthrich, MSc (corresponding author)
University of Applied Sciences and Arts
Northwestern Switzerland (FHNW
Institute of Thermal and Fluid Engineering (ITFE),
Klosterzelgstrasse 2, 5210 Windisch, Switzerland,
silas.wuethrich@fhnw.ch